

Local spin manipulation of quantized atomic currents

Martin Lebrat,¹ Samuel Häusler,¹ Philipp Fabritius,¹ Dominik Husmann,¹ Laura Corman,¹ and Tilman Esslinger¹

¹*Department of Physics, ETH Zurich, 8093 Zürich, Switzerland*

(Dated: Thursday 14th April, 2022, 18:54)

Spin is a fundamental quantum property of matter, and lifting its degeneracy lies at the heart of subtle transport phenomena and future schemes for quantum information processing. Here, we implement a microscopic spin filter for cold fermionic atoms in a quantum point contact (QPC) which allows us to create fully spin-polarized currents while retaining conductance quantization. Key to our scheme is a near-resonant optical tweezer which induces an effective Zeeman shift inside the QPC while its local character limits dissipation. We measure global effects of non-Hermitian evolution and interactions on the scale of the Fermi wavelength. Our work paves the way to studying hybrid mesoscopic structures combining spin-splitting and superfluidity far from equilibrium.

Coupling the spin of a particle to its motion unveils its quantum nature as was demonstrated in the Stern-Gerlach experiment [1]. On microscopic scales, this gives rise to fundamental transport phenomena: In metals or superconductors, magnetic impurities lead to a local coupling that strongly influences resistivity [2, 3]; in topological materials, a change in spin-orbit coupling across a boundary can induce spin-polarized edge modes [4] and Majorana fermions [5]. In this work, we use a quantum gas transport experiment [6] to explore spin manipulation on a length scale as short as the Fermi wavelength, where particle motion is quantum coherent. This regime is difficult to access in condensed-matter systems, yet it is at the center of new concepts for spintronics [7] and quantum computation [8]. Using a near-resonant optical tweezer inside an atomic transport channel, we realize an effective Zeeman splitting which is large compared to the Fermi energy and allows for an exquisite control of individual spin currents. As the laser acts only on a few atoms at a time we dramatically reduce dissipation caused by photon scattering, effectively increasing measurement times by several orders of magnitude compared to previous experiments optically coupling spin and motional degrees of freedom with alkali atoms [9–11].

We prepare a degenerate cloud of ⁶Li atoms in a thermal, balanced mixture of the first- and third-lowest hyperfine states, labeled as pseudo-spins $|\downarrow\rangle$ and $|\uparrow\rangle$, with about $N = 1.1(1) \cdot 10^5$ atoms per state at a typical temperature of $T = 66(12)$ nK. A magnetic field is tuned close to $B = 568$ G, where the collisional s -wave interactions between $|\downarrow\rangle$ and $|\uparrow\rangle$ vanish. We optically imprint a quantum point contact (QPC) with transverse confinement frequencies of $\nu_x = 14.0(6)$ kHz and $\nu_z = 9.03(5)$ kHz by intersecting two far-detuned repulsive laser beams. The QPC separates the cloud into two reservoirs that act as a source and drain of atoms with typical mean chemical potential $\mu_{\text{res}} = (\mu_L + \mu_R)/2 = k_B \cdot 0.23$ μK fixed by the total atom number. For a non-interacting Fermi gas, the conductance per spin and transverse QPC mode with unit transmission is equal to the conductance quantum $1/h$ [7]. The number of available transport modes is set via a far-detuned attractive beam with Gaussian waist $w_g = 31.8(3)$ μm . Its peak potential V_g is tunable and

augments the chemical potential μ_{res} locally to a value $V_g + \mu_{\text{res}}$ as depicted in Fig. 1A.

The control over each individual spin current is achieved using an additional σ^- -polarized beam centered on the QPC. Its Gaussian intensity profile is holographically defined by a Digital Micromirror Device and has a waist $w_s = 2.0(1)$ μm smaller than the typical Fermi wavelength $\lambda_F = \sqrt{h/mv_z} = 2.7$ μm , where m is the mass of a ⁶Li atom. Its optical frequency ν_s is tuned between the transition frequencies of $|\uparrow\rangle$ and $|\downarrow\rangle$ to the excited manifold $^2P_{3/2}$, inducing a repulsive dipole potential for $|\uparrow\rangle$ and an attractive potential for $|\downarrow\rangle$. For opposite detunings relative to the two transitions, i.e. $\delta_\uparrow = -\delta_\downarrow = 81.3$ MHz, both dipole potentials have equal magnitudes $\pm V_s$ linear in the light intensity I_s for $I_s \ll I_{\text{sat}}$, where $I_{\text{sat}} = 25.4$ W/m² is the saturation intensity of the transition. The induced lightshifts can be viewed as an optical analogue to the Zeeman shift $V_s = -\mu B_z$ of a spin-1/2 particle with magnetic moment μ in a fictitious magnetic field B_z . Unlike magnetically-induced shifts, atoms scatter photons at a rate Γ_s ; this imparts kinetic energy and leads to losses. The ratio Γ_s/V_s is independent of I_s and equal to 9.4 kHz/(k_B μK) for the detuning mentioned above [13].

Starting from a chemical potential bias across the QPC equal for both spins, we apply the spin-dependent optical potential to create a spin-polarized current. Typically, we prepare for each spin state atom number differences of $\Delta N(0) = 45(3) \cdot 10^3$ between the two reservoirs and measure their time evolution towards equilibrium. During that time, the s -wave scattering length is set to $a = 0(7) a_0$, where $a_0 = 52.9$ pm is the Bohr radius, and the optical power of the near-resonant tweezer is $P_s = 20(6)$ pW, corresponding to a peak intensity $I_s = 2P_s/\pi w_s^2 = 3(1)$ W/m² = 0.13(4) I_{sat} . Over 6 s, the relative atom number difference $\Delta N(t)/N(t)$ remains constant for spin $|\uparrow\rangle$ and is reduced by about one quarter for spin $|\downarrow\rangle$ with a fitted decay time of $\tau_\downarrow = 25(1)$ s (Fig. 1B). Assuming linear response, we infer currents for each spin of $I_\uparrow = -19 \pm 85$ atoms/s and $I_\downarrow = 833 \pm 98$ atoms/s. This corresponds to a fully spin-polarized current within fit error, comparable to the best values obtained with magnetic heterostructures [14].

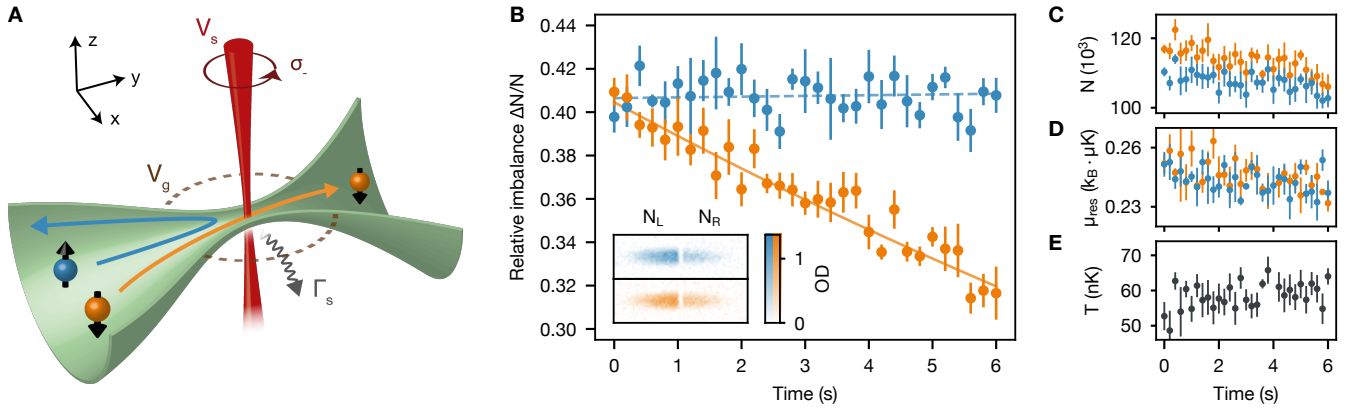


FIG. 1. **Creating spin-polarized currents through an atomic QPC.** (A) A near-resonant optical tweezer (red) with waist $w_s = 2.0(1) \mu\text{m}$ introduces an effective Zeeman shift V_s inside an optically-defined QPC (green). It allows ${}^6\text{Li}$ atoms in the lowest hyperfine state ($|\downarrow\rangle$, orange) to flow between two reservoirs while blocking atoms in the third-lowest state ($|\uparrow\rangle$, blue) thereby acting as a spin filter with losses determined by the photon scattering rate Γ_s . A far-detuned gate beam (dashed circle) locally increases the chemical potential μ_{res} imposed by the reservoirs by V_g . (B) Time evolution of the relative atom number difference between the left and right reservoirs $\Delta N/N = (N_L - N_R)/(N_L + N_R)$, obtained for a mean chemical potential $V_g + \mu_{\text{res}} = k_B \cdot 0.61(2) \mu\text{K}$, a near-resonant beam power $P_s = 20(6) \text{pW}$ and at a scattering length $a = 0(7) a_0$. It is constant for $|\uparrow\rangle$ and has a decay time of $25(1) \text{s}$ for $|\downarrow\rangle$. The associated currents $I_{\uparrow} = -19 \pm 85 \text{ atoms/s}$ and $I_{\downarrow} = 833 \pm 98 \text{ atoms/s}$ indicate fully polarized transport within fit error. Inset: Optical density (OD) after 6 s of left and right reservoirs over $970 \times 320 \mu\text{m}$, averaged over 5 absorption images. (C) Losses in atom number $N = N_L + N_R$ lead to a small variation of (D) mean reservoir chemical potential $\mu_{\text{res}} = (\mu_L + \mu_R)/2$. (E) Mean temperature $T = (T_L + T_R)/2$, constant over experimental timescales. Error bars show the standard error of the mean of 5 measurements.

Despite a maximal photon scattering rate $\Gamma_s = 3(1) \text{kHz}$ at the center of the tweezer, the decrease in total atom number N is limited (Fig. 1C) and smaller for spin $|\uparrow\rangle$ which is blocked by the spin-dependent potential. Losses lead overall to a decrease of the mean chemical potential $\mu_{\text{res}} = (\mu_L + \mu_R)/2$ in the reservoirs by $k_B \cdot 30 \text{nK}$ (Fig. 1D) much smaller than the other typical energy scales. Meanwhile, no significant increase of temperature T is observed (Fig. 1E). Since the atom-atom mean free path is larger than the system's size, the additional recoil energy $E_R = (h/\lambda)^2/2m = k_B \cdot 3.54 \mu\text{K}$ imparted to atoms scattered by near-resonant photons is not deposited in the reservoirs through thermalization. As currents and losses are small relative to the global atom number, we however expect the reservoirs to remain effectively described by thermal states [13].

The current polarization can be furthermore controlled by tuning the local chemical potential $V_g + \mu_{\text{res}}$ relative to the potentials experienced by both spins. We perform several measurements at weak scattering length $a = 91(7) a_0$ for different values of the gate potential V_g . The conductance is inferred by measuring the decay of the relative atom number difference $\Delta N/N$ after a fixed transport time of 4s [13]. If both spin energies are degenerate, we observe overlapping conductance plateaus for both spins which are characteristic of single-mode transport (Fig. 2A). Their value of $G = 0.84(1)/h$, slightly below the conductance quantum $1/h$, results from a reduction of the chemical potential bias between the reservoirs due to residual temperature differences, caused by

our initial preparation and omitted in the estimation of the conductance [13].

Upon increasing the near-resonant beam intensity I_s , the conductance plateau for the repelled spin $|\uparrow\rangle$ is shifted towards larger chemical potentials (Fig. 2B and C). This shift corresponds to the classical barrier $+V_s$ added to the QPC zero-point energy (Fig. 2D) by the spin-dependent potential (Fig. 2E and F, blue). An opposite shift is observed for the attracted spin $|\downarrow\rangle$, reflecting a weak decrease of the potential barrier due to the near-resonant beam being smaller than the wire length of $5.9(1) \mu\text{m}$ (Fig. 2E and F, orange). Current polarization is maximal for chemical potentials located between the potential barriers of both spins as in Fig. 1; the value of $V_g + \mu_{\text{res}} = k_B \cdot 0.61(2) \mu\text{K}$ chosen there is indicated by a dashed line in Fig. 2B and E. Strikingly, plateaus persist when increasing the intensity I_s to $0.17(5) I_{\text{sat}}$ while their value decreases down to $G = 0.55(2)/h$.

We expect transport observables such as conductance to be fundamentally robust against losses since they are sensitive only to scattering at energies close to the Fermi level which concerns a small fraction of all atoms subject to near-resonant light. In a Landauer picture valid for weak interactions, these losses contribute to decreasing the conductance by the scattering probability. For a typical Fermi velocity $v_F = \sqrt{h\nu_z/m} = 2.4 \text{cm/s}$ in the single-mode regime, that probability is equal to about 33% at $I_s = 0.17(5) I_{\text{sat}}$ and is consistent with the decrease of the conductance plateau from $G = 0.84(1)/h$ to $G = 0.55(2)/h$. In contrast, losses of atoms below the

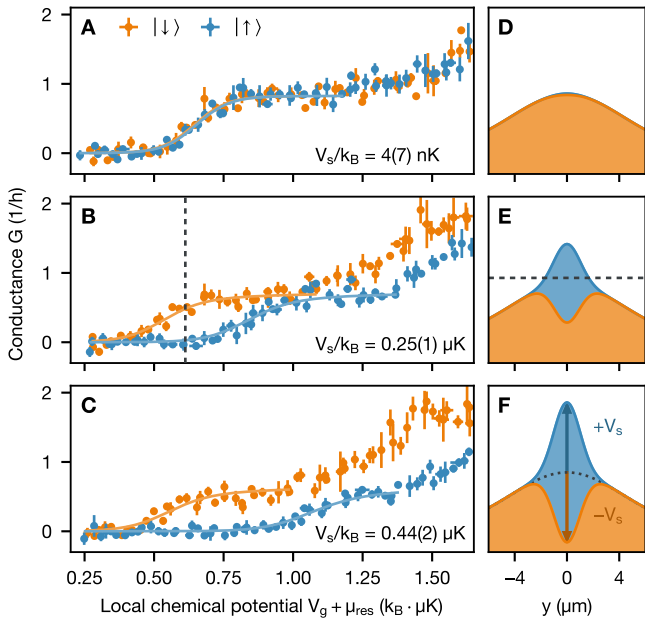


FIG. 2. **Lifting the spin degeneracy of the QPC ground state.** (A) Conductance G of each spin state at scattering length $a = 91(7) a_0$ versus local chemical potential $V_g + \mu_{\text{res}}$ without near-resonant beam; (B), with peak intensity $I_s = 0.13(4) I_{\text{sat}}$ (as in Fig. 1), where I_{sat} is the D_2 -line saturation intensity; (C) with $I_s = 0.17(5) I_{\text{sat}}$. Here and in the following, error bars correspond to the standard error of the mean of 3 measurements. Fits by a Landauer model are shown as solid curves and indicate an increase of the spin-dependent potential up to $V_s = k_B \cdot 0.44(2) \mu\text{K}$. (D), (E) and (F): Quasi-1D potentials along the transport direction y . The chemical potential of Fig. 1 is indicated as dashed lines in (B) and (E).

Fermi level do not generate a net current since their average velocity is zero. In the actual setup, these losses represent the majority of the losses shown in Fig. 1C [13] and only affect transport indirectly through the weak reduction of the chemical potential (Fig. 1D).

To extract the spin-dependent potential V_s , we fit the conductances of both states with a Landauer model (solid curves in Fig. 2A-C). The model describes the QPC and spin-dependent gate by two independent quasi-1D potentials shown in Fig. 2D-F, and includes a position-dependent photon scattering rate $\Gamma(y)$ as an imaginary part $i\hbar\Gamma(y)/2$ [13]. A linear regression on five different values of I_s yields a conversion ratio $V_s/I_s = 103(17) k_B \text{nK}/(\text{W}/\text{m}^2)$ compatible with the theoretical value of $98(3) k_B \text{nK}/(\text{W}/\text{m}^2)$. We find a maximal potential of $V_s = k_B \cdot 0.44(2) \mu\text{K}$, about twice the typical Fermi energy $E_F = \hbar\nu_z/2 = k_B \cdot 0.22 \mu\text{K}$ in the single-mode regime.

Including atom losses as an imaginary potential is a minimal way to capture non-Hermitian dynamics [15]. This model ignores the stochastic nature of the loss processes and applies well to particles described by a macro-

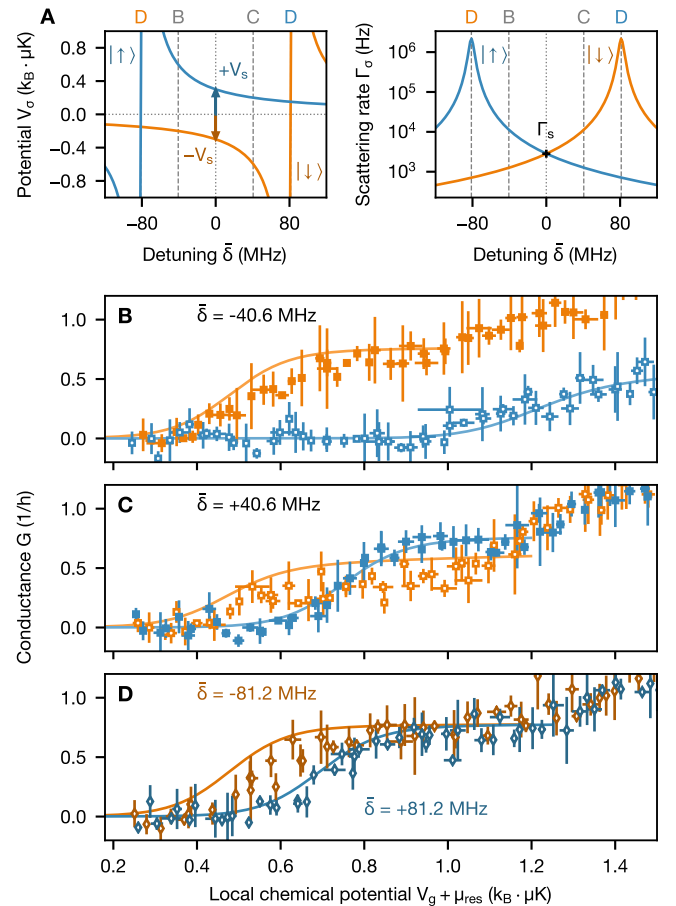


FIG. 3. **Validity of the Landauer model for large dissipation.** (A) Spin-dependent potential V_σ and scattering rate Γ_σ versus detuning $\bar{\delta}$ relative to the mean of the resonance frequencies $(\nu_\uparrow + \nu_\downarrow)/2$ for a light intensity $I_s = 0.13(4) I_{\text{sat}}$. $\pm V_s$ and Γ_s indicate the values obtained in Figs. 1 and 2B for $\bar{\delta} = 0$. (B) Conductance G at a scattering length $a = 91(7) a_0$ and detuning $\bar{\delta} = -40.6 \text{ MHz}$; (C) at detuning $\bar{\delta} = 40.6 \text{ MHz}$. (D) Blue (orange): conductance G for $|\uparrow\rangle$ ($|\downarrow\rangle$) with tweezer light on resonance with $|\downarrow\rangle$ ($|\uparrow\rangle$) at $\bar{\delta} = 81.3 \text{ MHz}$ (-81.3 MHz). Solid curves show a Landauer prediction using the fit parameters of Fig. 2B extended to different detunings.

scopic wavefunction, which may be adequate for condensed bosons [16, 17] but not necessarily for unpaired fermions [13]. To explore the validity range of this phenomenological model, we extend our conductance measurements to different tweezer detunings $\bar{\delta}$ relative to the mean resonance frequency $(\nu_\uparrow + \nu_\downarrow)/2$ at fixed intensity $I_s = 0.13(4) I_{\text{sat}}$. As shown in Fig. 3A, this affects both spin-dependent dipole potential V_σ and photon scattering rate Γ_σ , and allows to change the latter by more than three orders of magnitude. Tuning the frequency by $\bar{\delta} = -40.6 \text{ MHz}$ towards the resonance of $|\uparrow\rangle$ leads to a shift of the conductance curve towards higher chemical potentials (Fig. 3B, blue), since the repulsive potential barrier and scattering rate for that state are increased. Meanwhile, the conductance of $|\downarrow\rangle$ (Fig. 3B,

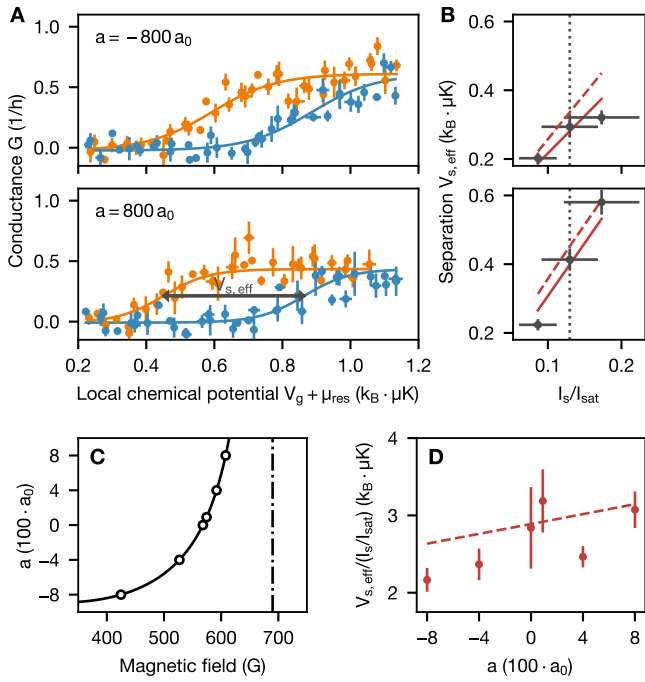


FIG. 4. Effect of 1D interactions on transport. (A) Conductance G at scattering lengths $a = -800.0(7) a_0$ and $a = +800(16) a_0$, near-resonant beam intensity $I_s = 0.13(4) I_{\text{sat}}$ and equal detuning from both states, $\bar{\delta} = 0$. Solid curves indicate fits with a logistic function to extract the energy separation $V_{s,\text{eff}}$. (B) Fitted separation $V_{s,\text{eff}}$ versus I_s normalized by the D_2 -line saturation intensity I_{sat} . The vertical dotted line indicates the intensity used in (A). (C) Scattering length a versus magnetic field, tuned to the left of a broad Feshbach resonance (dash-dotted line) and calibrated within 0.1%. (D) Ratio $V_{s,\text{eff}}/(I_s/I_{\text{sat}})$ versus scattering length a , obtained by linear regression displayed as solid lines in (B). A Hartree mean-field model including a finite temperature of 66 nK is indicated as dashed lines in (B) and (D).

orange) approaches the one measured in the absence of near-resonant light (Fig. 2A). The reverse trend is observed with a detuning $\bar{\delta} = +40.6$ MHz, where the conductance of $|\downarrow\rangle$ is clearly reduced due to increased losses (Fig. 3C). These measurements show good agreement with the previous Landauer model, without refitting the data and only converting V_s and Γ_s obtained in Fig. 2B to different detunings. Finally, bringing the tweezer on resonance with one of the two states leads to its entire loss after 4 s, while the other non-resonant state still displays quantized conductance (Fig. 3D). The applicability of Landauer theory here highlights that the coupling between spins is negligible at this scattering length.

Interactions between spins have previously been studied in the context of diffusive spin transport in the bulk of interacting Fermi gases [4, 18–21, 23, 24] as well as in Bose- [25] and Fermi-Hubbard [26] systems. Using the broad Feshbach resonance of ^6Li , we study here how the effective Zeeman shift V_s competes with the new en-

ergy scale introduced by interactions within the optical tweezer, where only up to two atoms are typically present. We explore both attractive and repulsive interactions from $a = -800.0(7) a_0$ to $800(16) a_0$ in the non-superfluid regime. Fig. 4A shows conductances for each spin obtained at $a = \pm 800 a_0$, equal detunings to their resonances $\bar{\delta} = 0$, and fixed intensity $I_s = 0.13(4) I_{\text{sat}}$ as a function of the local chemical potential $V_g + \mu_{\text{res}}$. We observe a change in the energy separation $V_{s,\text{eff}}$ between the conductance curves, as well as a reduction of the conductance values compared to Fig. 2B which we attribute to slightly increased losses. This separation is visibly reduced for attractive interactions and increased for repulsive interactions. We quantify it with a fit by a logistic function motivated by non-interacting Landauer theory for different values of I_s (Fig. 4B). The different slopes $V_{s,\text{eff}}/(I_s/I_{\text{sat}})$, obtained by linear regression, confirm the effect of interactions.

We repeat this measurement for intermediate scattering lengths a (Fig. 4C) and extract the ratio $V_{s,\text{eff}}/(I_s/I_{\text{sat}})$ for each interaction strength (Fig. 4D). The data is described by a self-consistent Hartree mean-field model [13] where $|\downarrow\rangle$ -atoms provide an extra potential proportional to the interaction parameter $U = 2h\sqrt{\nu_x\nu_z}a$ that ease or hinder the passage of $|\uparrow\rangle$ -atoms depending on its sign. We find a good agreement even though the model does not include dissipation and density fluctuations which are expected to be large in the 1D region. Crucially, our conductance signal is obtained by probing the QPC with typically a few thousand atoms over 4 s, which averages out these fluctuations and allows us to measure a mean-field shift. Many-body correlations are expected to be more sensitive to dissipation than particle densities.

Our work demonstrates how transport measurements can detect minute density variations on the scale of the Fermi wavelength from the integration of a weak transport signal. Our capability to spin-engineer potentials can be readily extended to more complex structures [27] and opens avenues for exploring the transport dynamics of strongly-correlated systems, where novel nonequilibrium spin and heat transport [28, 29] and exotic phases of matter [5] could be observed.

ACKNOWLEDGMENTS

We thank L. Bartha for early theoretical and technical contributions; T. Giamarchi, L. Glazman, H. Moritz, H. Ott and A.-M. Visuri for helpful discussions; and J.-P. Brantut, R. Citro, M. Landini, J. Mohan, and K. Viebahn for their critical reading of the manuscript. We acknowledge the Swiss National Science Foundation (Project n° 182650 and NCCR-QSIT) and ERC advanced grant TransQ (Project n° 742579) for funding. L.C. is supported by ETH Zurich Postdoctoral Fellowship, Marie Curie Actions for People COFUND program and ERC Marie Curie TopSpiD (Project n° 746150).

-
- [1] W. Gerlach and O. Stern, *Der experimentelle Nachweis der Richtungsquantelung im Magnetfeld*, *Zeitschrift für Physik* **9**, 349 (1922).
- [2] J. Kondo, *Resistance Minimum in Dilute Magnetic Alloys*, *Progress of Theoretical Physics* **32**, 37 (1964).
- [3] H. Shiba, *Classical Spins in Superconductors*, *Progress of Theoretical Physics* **40**, 435 (1968).
- [4] C. L. Kane and E. J. Mele, *\mathbb{Z}_2 Topological Order and the Quantum Spin Hall Effect*, *Physical Review Letters* **95**, 146802 (2005).
- [5] C. Beenakker, *Search for Majorana Fermions in Superconductors*, *Annual Review of Condensed Matter Physics* **4**, 113 (2013).
- [6] S. Krinner, T. Esslinger, and J.-P. Brantut, *Two-terminal transport measurements with cold atoms*, *Journal of Physics: Condensed Matter* **29**, 343003 (2017).
- [7] I. Žutić, J. Fabian, and S. Das Sarma, *Spintronics: Fundamentals and applications*, *Reviews of Modern Physics* **76**, 323 (2004).
- [8] D. Loss and D. P. DiVincenzo, *Quantum computation with quantum dots*, *Physical Review A* **57**, 120 (1998).
- [9] Y.-J. Lin, K. Jiménez-García, and I. B. Spielman, *Spin-orbit-coupled Bose-Einstein condensates*, *Nature* **471**, 83 (2011).
- [10] P. Wang, Z.-Q. Yu, Z. Fu, J. Miao, L. Huang, S. Chai, H. Zhai, and J. Zhang, *Spin-Orbit Coupled Degenerate Fermi Gases*, *Physical Review Letters* **109**, 095301 (2012).
- [11] L. W. Cheuk, A. T. Sommer, Z. Hadzibabic, T. Yefsah, W. S. Bakr, and M. W. Zwierlein, *Spin-Injection Spectroscopy of a Spin-Orbit Coupled Fermi Gas*, *Physical Review Letters* **109**, 095302 (2012).
- [7] S. Krinner, D. Stadler, D. Husmann, J.-P. Brantut, and T. Esslinger, *Observation of quantized conductance in neutral matter*, *Nature* **517**, 64 (2015).
- [13] Materials and methods are available as supplementary material.
- [14] C. H. Marrows, *Spin-polarised currents and magnetic domain walls*, *Advances in Physics* **54**, 585 (2005).
- [15] N. Moiseyev, *Non-Hermitian Quantum Mechanics* (Cambridge University Press, 2011).
- [16] I. Carusotto and C. Ciuti, *Quantum fluids of light*, *Reviews of Modern Physics* **85**, 299 (2013).
- [17] G. Barontini, R. Labouvie, F. Stubenrauch, A. Vogler, V. Guarrera, and H. Ott, *Controlling the Dynamics of an Open Many-Body Quantum System with Localized Dissipation*, *Physical Review Letters* **110**, 035302 (2013).
- [18] X. Du, Y. Zhang, J. Petricka, and J. E. Thomas, *Controlling Spin Current in a Trapped Fermi Gas*, *Physical Review Letters* **103**, 010401 (2009).
- [19] A. Sommer, M. Ku, G. Roati, and M. W. Zwierlein, *Universal spin transport in a strongly interacting Fermi gas*, *Nature* **472**, 201 (2011).
- [20] M. Koschorreck, D. Pertot, E. Vogt, and M. Köhl, *Universal spin dynamics in two-dimensional Fermi gases*, *Nature Physics* **9**, 405 (2013).
- [21] A. B. Bardou, S. Beattie, C. Luciuk, W. Cairncross, D. Fine, N. S. Cheng, G. J. A. Edge, E. Taylor, S. Zhang, S. Trotzky, and J. H. Thywissen, *Transverse Demagnetization Dynamics of a Unitary Fermi Gas*, *Science* **344**, 722 (2014).
- [4] S. Krinner, M. Lebrat, D. Husmann, C. Grenier, J.-P. Brantut, and T. Esslinger, *Mapping out spin and particle conductances in a quantum point contact*, *Proceedings of the National Academy of Sciences* **113**, 8144 (2016).
- [23] C. Luciuk, S. Smale, F. Böttcher, H. Sharum, B. Olsen, S. Trotzky, T. Enss, and J. Thywissen, *Observation of Quantum-Limited Spin Transport in Strongly Interacting Two-Dimensional Fermi Gases*, *Physical Review Letters* **118**, 130405 (2017).
- [24] G. Valtolina, F. Scazza, A. Amico, A. Burchianti, A. Recati, T. Enss, M. Inguscio, M. Zaccanti, and G. Roati, *Exploring the ferromagnetic behaviour of a repulsive Fermi gas through spin dynamics*, *Nature Physics* **13**, 704 (2017).
- [25] T. Fukuhara, A. Kantian, M. Endres, M. Cheneau, P. Schauß, S. Hild, D. Bellem, U. Schollwöck, T. Giamarchi, C. Gross, I. Bloch, and S. Kuhr, *Quantum dynamics of a mobile spin impurity*, *Nature Physics* **9**, 235 (2013).
- [26] M. A. Nichols, L. W. Cheuk, M. Okan, T. R. Hartke, E. Mendez, T. Senthil, E. Khatami, H. Zhang, and M. W. Zwierlein, *Spin transport in a mott insulator of ultracold fermions*, *Science* (2018), 10.1126/science.aat4387.
- [27] M. Lebrat, P. Grišins, D. Husmann, S. Häusler, L. Cormann, T. Giamarchi, J.-P. Brantut, and T. Esslinger, *Band and Correlated Insulators of Cold Fermions in a Mesoscopic Lattice*, *Physical Review X* **8**, 011053 (2018).
- [28] G. E. W. Bauer, E. Saitoh, and B. J. v. Wees, *Spin caloritronics*, *Nature Materials* **11**, 391 (2012).
- [29] F. S. Bergeret, M. Silaev, P. Virtanen, and T. T. Heikkilä, *Colloquium: Nonequilibrium effects in superconductors with a spin-splitting field*, *Reviews of Modern Physics* **90**, 041001 (2018).

MATERIALS AND METHODS

Experimental details

Experimental cycle

In brief, a balanced mixture of the lowest and third-lowest hyperfine state is loaded into a hybrid trap with transverse frequencies $\nu_{\text{trap},x} = 122(3)$ Hz and $\nu_{\text{trap},z} = 110(3)$ Hz along x and z provided by a 1064 nm optical dipole trap, and longitudinal frequency $\nu_{\text{trap},y}$ along y produced by a magnetic trap which ranges from 22 to 27 Hz depending on the background magnetic field used during transport. Typical temperatures of 66(12) nK which correspond to $T/T_F = 0.24(2)$ are prepared by evaporative cooling at the s -wave scattering length $a = -776 a_0$. Subsequently the magnetic field is tuned to a value of 568 G in Fig. 1, at 574 G in Figs. 2 and 3, and between 425 G and 608 G in Fig. 4. The magnetic field is calibrated separately by measuring losses due to three-body collisions close to narrow s - and p -wave resonances whose positions are determined in [S1].

Transport is induced by a chemical potential bias created by displacing the center of the underlying magnetic trap with a magnetic field gradient, splitting the cloud into two asymmetric reservoirs with an elliptical repulsive beam, and finally re-centering the magnetic trap. Two additional TEM₀₁-shaped beams at 532 nm confine atoms at the cloud center along the x and z directions into a quantum point contact (QPC), with respective Gaussian waists $w_x = 5.9(1)$ μm and $w_z = 30.2$ μm in transport direction y . Transport is allowed through the QPC by switching off the elliptical beam for 4 s in Figs. 2-4. Atom numbers, chemical potential and temperatures for each reservoir are finally computed from the density distribution obtained from absorption pictures along the x -direction after a time of flight of 1 ms.

Shaping and alignment of the near-resonant beam

A Digital Micromirror Device (DMD DLP7000 0.7" XGA from Texas Instruments; Driver Vialux V7000) is used to precisely shape a Gaussian beam of wavelength $\lambda = 671$ nm onto the QPC. The DMD is a rectangular array of 1024×768 micron-scale mirrors which can be individually controlled, thereby forming a reflective diffraction grating. The grating imprints an amplitude and phase hologram on the near-resonant beam, whose Fourier transform is optically conjugated to the (x, y) plane of the QPC with a set of relay lenses and a high-resolution microscope. The shape and extent of the beam are imaged using a second microscope placed symmetrically after the QPC. Aberrations introduced by the optical setup are corrected with the DMD via a technique similar to a Hartmann-Shack analysis.

To center the near-resonant beam onto the QPC center

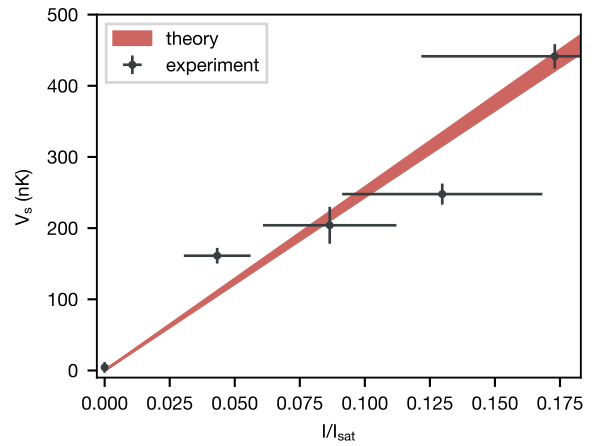


FIG. S1. **Calibration of the spin-dependent potential.** Spin-dependent potential V_s versus intensity I_s normalized by saturation intensity I_{sat} , fitted from the conductance curves of Fig. 2 (black circles) and calculated ab initio (red area). The horizontal and vertical error bars of the experimental points correspond to the calibration uncertainty on I_s and the fit error on V_s respectively. The error on the theory line includes calibration uncertainties on the detuning and polarization of the near-resonant beam.

in the (x, y) plane, we increase the dissipation rate for spin $|\downarrow\rangle$ by detuning it closer to its resonance, and map out losses as a function of the beam position, realizing a dissipative analog to a scanning gate microscope [S2]. We also ensure that parasitic diffraction orders that could reach the atoms are adequately blocked.

Intensity and spin-dependent potential calibration

We measure the Gaussian waist $w_s = 2.0(1)$ μm of the near-resonant tweezer in the transport direction with the second microscope used to quantify optical aberrations. To calibrate its intensity we precisely characterize several neutral density filters that attenuate the beam power to the picowatt range. These filters are calibrated by imaging the beam with a camera at different powers and exposures on the one hand; and by directly measuring the decrease in beam power due to the filters at higher absolute powers on the other hand. We deduce an attenuation by 3.4(1) orders of magnitude whose large uncertainty is the main source of systematic error in estimating the beam intensity.

The spin potential V_s measured in Fig. 2 increases with beam intensity I_s , as shown in Fig. S1. As I_s is small compared to the saturation intensity $I_{\text{sat}} = 25.4 \text{ W/m}^2$, V_s is expected to be linear in I_s . An orthogonal-distance regression [S3] yields a slope of 103(17) nK/(W/m²). It is compatible within one standard error with a theoretical value of 98(3) nK/(W/m²) independently calculated via (S12) and our knowledge of the polarization, detuning, and magnetic field.

Data analysis

Conductance without temperature difference

In the absence of a temperature difference $\Delta T = 0$, the particle current through the QPC is linear in the chemical potential between the reservoirs:

$$I_N = G\Delta\mu \quad (\text{S1})$$

where G is the conductance of the channel. The linear approximation is valid for the weak interaction strengths considered here [S4]. This further ensures that spin drag is negligible and that biases, currents, and transport coefficients can be treated independently for each spin $\sigma \in \{\uparrow, \downarrow\}$ (omitted in the following).

The chemical potential for each reservoir $r \in \{L, R\}$ and each spin can be furthermore expanded to first order around the atom number at $t = 0$, $d\mu_r = dN_r/\kappa_r$, where κ_r is the compressibility of one reservoir. Eq. (S1) can then be simplified to a closed first order differential equation in the atom number difference ΔN . This difference is therefore an exponentially decreasing function of time with a time constant

$$\tau = G \left(\frac{1}{\kappa_L} + \frac{1}{\kappa_R} \right) \approx \frac{2G}{\kappa} \quad (\text{S2})$$

where we replace reservoir compressibilities at $t = 0$ by the reservoir compressibility κ at global equilibrium for a mean atom number $\bar{N} = (N_L + N_R)/2$ and temperature T , without significant change in the results. This represents the analogue of an RC circuit for neutral atoms, replacing charge by the number of atoms transferred from one reservoir to the other $\Delta N/2$, and capacitance by the compressibility per reservoir κ .

In Figs. 2-4, the time constant τ for each spin state is inferred from the atom number difference after a fixed transport time t

$$\tau = -t \ln \frac{\Delta N(t)}{\Delta N(0)}. \quad (\text{S3})$$

We calibrate the initial value $\Delta N(0)$ for each set of experimental parameters (scattering length, near-resonant beam intensity and detuning) by averaging $\Delta N(t)$ for low values of the gate potential V_g , when transport is absent. Together with the reservoir compressibility κ , Eq. (S2) allows us deduce the conductance G .

Effect of a temperature difference

In practice, initial temperature differences ΔT are inherent to our preparation of a chemical potential difference, which requires a shift of the magnetic trap along y that adiabatically compresses the left reservoir and expands the right reservoir. Thermoelectric effects are captured by Onsager's transport theory relating particle

current to the chemical potential and temperature differences $\Delta\mu$ and ΔT between the reservoirs:

$$I_N = G\Delta\mu + G\alpha_c\Delta T \quad (\text{S4})$$

$$= G/\kappa \cdot \Delta N + G(\alpha_c - \alpha_r) \cdot \Delta T \quad (\text{S5})$$

introducing here the Seebeck coefficient of the channel α_c . Eq. (S5) is obtained from (S4) by linearly expanding $\Delta\mu$ in ΔN and ΔT via the compressibility κ and the dilatation coefficient α_r of one reservoir at equilibrium. At low temperatures in the single-mode regime, the thermocurrent proportional to the Seebeck term α_c can be neglected compared to the reservoir contribution proportional to $\alpha_r \approx 1.4k_B$. For typical values of κ and $\Delta N = 40 \cdot 10^3$, the second term of (S5) leads to a 15% reduction of the particle current for temperature differences as little as $\Delta T = 10$ nK. This effect can therefore explain the decrease of the conductance plateau below the quantum $1/h$ to $G = 0.85(1)/h$, observed in Fig. 2 without the near-resonant tweezer.

Independent measurements of the temperature yield a positive value $\Delta T = 35 \pm 24$ nK larger but compatible with the estimate stated above. Owing to the large statistical uncertainty on ΔT , we decide to use Eqs. (S2) and (S3) for estimating conductance based on ΔN only and to include temperature effects as a scaling factor reducing the conductance obtained via our Landauer model.

Extracting thermodynamic quantities from the cloud profile

Extracting the conductance relies on the knowledge of the temperature, the atom number and the compressibility for each half-reservoir and each internal state. To that end, we rely on the equation of state of non-interacting Fermi gases. The atomic cloud is imaged after a short time-of-flight during which it only expands along the tight confinement axes x, z . We integrate the density distribution along these axes and extract the second moment of the distribution along the weakly confined axis y . This second moment can be related to the total energy of the gas thanks to the virial theorem for non-interacting Fermi gases. The non-interacting equation of state allows to deduce the other relevant thermodynamic quantities such as chemical potential, temperature and reservoir compressibility. We verified that the extracted quantities do not differ significantly from those obtained with an interacting equation of state in the mean-field limit [S5] for the weak scattering lengths $|a| < 800 a_0$ used here.

Fitting procedure

The conductance shown in Figs. 2 and 3 as a function of the local chemical potential $V_g + \mu_{\text{res}}$ is compared to the results of a Landauer model including dissipation presented in a later section. The relevant model parameters

are summarized by the following function

$$y_\sigma(x) = AG_\sigma(x - \mu_0, T, \bar{\delta}, V_s), \quad (\text{S6})$$

where G_σ is obtained via (S23), A is a scaling factor capturing the decrease of the extracted conductance below $1/h$ due to the temperature difference, μ_0 is a chemical potential offset, T is the temperature, $\bar{\delta}$ is the detuning relative to the mean resonance frequency and V_s is the magnitude of the spin-dependent potential at $\bar{\delta} = 0$.

In Fig. 2, all points ($V_g + \mu_{\text{res}}, G_\sigma$) associated with the same near-resonant beam intensity I_s are fitted with (S6) for both spins σ simultaneously. We use A , μ_0 and V_s as free parameters, fix T to the mean temperature independently measured from the cloud density profiles, and fix $\bar{\delta}$ to 0. The fitted values of V_s and fit errors are reported in the main text. The fitted scale A is about 0.8 for all I_s and is consistent with the estimation obtained from (S5), while the chemical potential offset μ_0 is consistently below $k_B \cdot 0.1 \mu\text{K}$, hinting at minor technical imperfections of the QPC potential or a small systematical error in the calibration of the QPC beams.

In Fig. 3, we plot the Landauer-Büttiker model (S6) for different detunings $\bar{\delta}$. The parameters A , μ_0 and V_s are fixed to the values obtained in Fig. 2 at $I = 0.13I_s$ and T is set to the mean temperature extracted in Fig. 2.

In Fig. 4A, ($V_g + \mu_{\text{res}}, G_\sigma$) is fitted for both spin states σ simultaneously with the following function:

$$y_\sigma(x) = \frac{A}{1 + \exp[-(x - \mu_{0,\sigma})/w]} + B \quad (\text{S7})$$

with a common amplitude A , width w , and vertical offset B , and independent chemical potential shifts $\mu_{0,\sigma}$ for the two spins. The horizontal separation between the two curves is defined as $V_{s,\text{eff}} = \mu_{0,\uparrow} - \mu_{0,\downarrow}$. In Fig. 4B, $V_{s,\text{eff}}$ is then plotted versus the normalized beam intensity I_s/I_{sat} and fitted with a linear function $y(x) = Ax$.

All fits described above are performed by orthogonal distance regression [S3] to include errors along x and y .

DIPOLE POTENTIAL AND SCATTERING RATE

Estimating dipole potentials and scattering rates requires a precise knowledge of the frequencies and dipole moments of all optical transitions and therefore of the eigenvalues and eigenstates of the magnetic field-dependent Hamiltonian describing the internal states of a single atom.

The experiment is carried out at strong magnetic fields \vec{B} where the energy of the electron's magnetic dipole moment exceeds the hyperfine interaction for ${}^6\text{Li}$. In this Paschen-Back regime, the lowest and third-lowest hyperfine states used in the experiment are well described by their electronic spin $m_J = -1/2$ and nuclear spin $m_I = +1$ and -1 respectively. The single-atom Hamiltonian can be expressed as a function of the electronic and nuclear

spin operators $\hat{J} = \hat{L} + \hat{S}$ and \hat{I}

$$\hat{H}_{\text{at}} = \frac{\mu_B}{\hbar}(g_J \hat{J} \cdot \vec{B} + g_I \hat{I} \cdot \vec{B}) + \frac{a}{\hbar^2} \hat{J} \cdot \hat{I}, \quad (\text{S8})$$

where μ_B is the Bohr magneton, g_J and g_I the electronic and nuclear gyromagnetic factors, and a the hyperfine coupling energy. Both g_J and a depend on the electron's orbital momentum L and total spin S which characterize each level manifold $2S$, $2P_{1/2}$, and $2P_{3/2}$. Their values for ${}^6\text{Li}$ are reported in [S6].

The dipole matrix element between two states labeled by electron and nuclear spin (J, m_J, m_I) is given by the Wigner-Eckardt theorem:

$$d_{kk'}^q = \frac{1}{\sqrt{2J'+1}} \delta_{m_I, m_I'} \langle Jm_J, 1q | J'm_J' \rangle \langle J' || \vec{d} || J \rangle, \quad (\text{S9})$$

where $\langle Jm_J, 1q | J'm_J' \rangle$ is the Clebsch-Gordan coefficient relating initial and final electron spins m_J and m_J' through the added angular momentum $q = -1, 0, +1$ of a photon with polarization σ^-, π, σ^+ , and $\langle J' || \vec{d} || J \rangle$ is the reduced matrix element of the corresponding $2S \rightarrow 2P$ transition. The dipole matrix elements d_{eg}^q between each pair of eigenstates $|g\rangle$ and $|e\rangle$ of (S8) are then given via a change of basis.

These dipole matrix elements appear in the complex polarizability tensor of each state $|g\rangle$ of the ground manifold $2S$ at light frequency ν :

$$\alpha_g^{qq'} = - \sum_e \frac{(d_{eg}^q)^* d_{eg}^{q'}}{h(\nu - \nu_{eg}) + i\hbar\Gamma_{eg}/2}, \quad (\text{S10})$$

where the sum runs over all excited states $|e\rangle$ in $2P_{1/2}$ and $2P_{3/2}$. The transition frequencies ν_{eg} between ground and excited states are derived from the eigenvalues of (S8), and Γ_{eg} denotes the spontaneous emission rates from excited to ground states:

$$\Gamma_{eg} = \frac{(h\nu_{eg})^3}{3\pi\epsilon_0 c^3 \hbar^4} \sum_q |d_{eg}^q|^2, \quad (\text{S11})$$

where c is the speed of light and ϵ_0 is the vacuum permittivity.

For light intensities I small compared to the saturation intensity, the light shift V and scattering rate Γ experienced in the ground state $|g\rangle$ are related to the dispersive and dissipative parts of the polarizability:

$$V = - \frac{I}{2\epsilon_0 c} \sum_{q,q'} e_q \text{Re}(\alpha_g^{qq'}) e_{q'}^* \quad (\text{S12})$$

$$\Gamma = \frac{I}{\hbar\epsilon_0 c} \sum_{q,q'} e_q \text{Im}(\alpha_g^{qq'}) e_{q'}^* \quad (\text{S13})$$

The sum indicates a double tensor contraction by the light polarization $\vec{e} = \vec{E}/|\vec{E}| = \sum_q e_q \vec{u}_q$, whose coordinates are expressed here in the basis $\vec{u}_{-1} = (\vec{u}_x - i\vec{u}_y)/\sqrt{2}$ for

σ^- -polarization, $\vec{u}_0 = \vec{u}_z$ for π -polarization, and $\vec{u}_{+1} = (\vec{u}_x + i\vec{u}_y)/\sqrt{2}$ for σ^+ -polarization.

In this work, Eqs. (S12) and (S13) are evaluated for σ^- -polarization at frequencies close to the transitions from the $\{2S, m_J = -1/2\}$ to the $\{2P_{3/2}, m_J = -3/2\}$ manifolds, which are closed transitions provided that admixtures to $\{2S, m_J = +1/2\}$ and $\{2P_{3/2}, m_J = -1/2\}$ states via hyperfine coupling are negligible.

RESERVOIR DYNAMICS

Single-atom dynamics

The near-resonant beam is responsible for local photon scattering inside the QPC. In Figs. 1 and 2B, the center intensity of the near-resonant optical tweezer $I_s = 3(1) \text{ W/m}^2$ is associated with a photon absorption rate $\Gamma = 3.1(9) \text{ kHz}$. Atoms moving at the Fermi velocity $v_F = \sqrt{h\nu_z/m} = 2.4 \text{ cm/s}$ pass through the near-resonant beam in a typical time $t_F = w_s/v_F = 81 \mu\text{s}$; meanwhile, a fraction Γt_F of about 25 % absorbs a photon. This fraction increases up to 33 % for the maximal intensity $I_s = 4(1) \text{ W/m}^2$ as stated in the main text. This classical estimation does not include the dipole potential created by the near-resonant beam, which affects the local atomic velocity and density and results in spin-dependent losses visible in Fig. 1C.

Atoms that absorb a photon re-emit it spontaneously at a rate $\Gamma_0 = 36.9 \text{ MHz}$ during which they move by less than one nanometer. The imparted recoil energy $E_R = (h/\lambda)^2/2m = k_B \cdot 3.54 \mu\text{K} = h \cdot 73.7 \text{ kHz}$ is smaller than the potential barrier imposed by the confining beams, equal to $k_B \cdot 48 \mu\text{K}$ in the z direction and $k_B \cdot 7 \mu\text{K}$ in the x direction. Atoms therefore do not escape the QPC laterally and are projected to a superposition of transverse QPC modes, described by the Lamb-Dicke parameter $\eta_z = \sqrt{E_R/h\nu_z} = 2.86(1)$ for a recoil momentum transfer along z and $\eta_x = \sqrt{E_R/h\nu_x} = 2.29(4)$ along x . They are however directed towards the reservoirs along the non-confined direction y . Since the recoil energy is larger than the depth $U = k_B \cdot 0.55 \mu\text{K}$ of the optical trap defining the reservoirs, scattered atoms eventually escape the system and do not contribute to a global energy increase for the weakest interactions, where their mean free path is larger than the reservoir size.

Thermalization

Thermalization in the reservoirs is determined by the atom-atom scattering time which can be approximated as $\tau_s = 1/\bar{n}\sigma v_F$, where \bar{n} is the peak density at the trap center, σ is the interatomic scattering cross-section and v_F the Fermi velocity. This estimation is an upper bound since it neglects Pauli blocking which suppresses scattering by a factor T/T_F . For s -wave scattering lengths

$|a| > 91 a_0$ as explored in Figs. 2-4, the scattering time is smaller than 0.4 s and therefore shorter than the typical decay times of the relative imbalance by more than one order of magnitude.

In Fig. 1, s -wave interactions are set to zero within experimental uncertainty to ensure that atom losses are ascribed to photon scattering from the near-resonant beam only, allowing us to describe them with the quantitative model presented in the next section. Even though this assumption should formally break down, we expect the reservoirs to remain approximated by thermal states since atom number variations due to transport and losses are smaller than 10% per reservoir. For all practical purposes, we do not measure a significant difference between the chemical potentials μ_{res} and temperatures T effectively extracted from the data of Fig. 1 at $a = 0(7) a_0$ and Fig. 2 at $a = 91(7) a_0$ via the same processing procedure relying on the assumption of thermalized reservoirs. Such an agreement between observables in thermalized and non-thermalized regimes was already noted in our previous experimental work [S7], and is furthermore supported by theoretical studies on the validity of the Landauer formalism both in presence of incoherent baths or in a complete microcanonical picture [S8].

LANDAUER MODEL WITH DISSIPATION

Effective Hamiltonian with losses

For a system evolving according to a Hamiltonian \hat{H}_0 which is weakly coupled to a fast evolving environment (Born-Markov approximation), the evolution of the density matrix ρ is determined by a master equation:

$$\partial_t \hat{\rho} = -\frac{i}{\hbar} [\hat{H}, \hat{\rho}] - \sum_j \left(\frac{1}{2} \hat{L}_j^\dagger \hat{L}_j \hat{\rho} + \frac{1}{2} \hat{\rho} \hat{L}_j^\dagger \hat{L}_j - \hat{L}_j \hat{\rho} \hat{L}_j^\dagger \right) \quad (\text{S14})$$

where \hat{L}_j represent the jump operators describing the loss processes and is proportional to the square root of the scattering rate (S13). The first two terms of the sum can be included in the commutator by defining an effective, complex-valued Hamiltonian

$$\hat{H}_{\text{eff}} = \hat{H}_0 - i \frac{\hbar}{2} \sum_j \hat{L}_j^\dagger \hat{L}_j \quad (\text{S15})$$

which becomes for losses spatially varying along y :

$$\hat{H}_{\text{eff}} = \hat{H}_0 - i \frac{\hbar \Gamma(y)}{2} \hat{\Psi}^\dagger(y) \hat{\Psi}(y) \quad (\text{S16})$$

The last term in the sum of (S14) represents fluctuations and is necessary to preserve fermionic commutation relations. Since our observables are macroscopic response functions measured over times very large compared to the fluctuation timescales, we model losses here using the effective Hamiltonian (S16) only.

Transmission and loss coefficients

In the ballistic regime, the conductance between the two reservoirs at chemical potentials μ_L and μ_R only depends on the overall transmission at a given energy E :

$$\mathcal{T}(E) = \sum_{\text{modes } \mathbf{n}} \mathcal{T}_{\mathbf{n}}(E) \quad (\text{S17})$$

where $\mathcal{T}_{\mathbf{n}}(E)$ is the transmission of mode \mathbf{n} , i.e. the average probability that a particle injected at one end with energy E will be transmitted to the other end.

Transport modes correspond here to different harmonic transverse modes $\mathbf{n} = (n_x, n_z)$ which have significant transmission for energies E that are larger than their harmonic energy at the center of the QPC $E_{\mathbf{n}} = h\nu_x(n_x + 1/2) + h\nu_z(n_z + 1/2)$. Furthermore, we experimentally observe that the second conductance mode (expected to appear at local chemical potentials $V_g + \mu_{\text{res}} \approx k_B \cdot 1 \mu\text{K}$) has a nearly vanishing transmission and therefore does not contribute to transport.

In the following, we therefore restrict our analysis to the first conductance mode $\mathbf{n} = (0, 0)$, which is valid at low chemical potentials. Its associated potential landscape consists of:

1. the space-dependent zero-point energy due to the x - and z -confinement

$$V_0(y) = \frac{1}{2}h\nu_z e^{-y^2/w_z^2} + \frac{1}{2}h\nu_x e^{-y^2/w_x^2} \quad (\text{S18})$$

where $\nu_{x,z}$ are the maximum confinement frequencies and $w_{x,z}$ the waists along y of the beams providing this confinement;

2. the spin-dependent potential $V_{\sigma}(y)$ defined by (S12) and proportional to the near-resonant beam intensity $I(y) = I_s e^{-2y^2/w_s^2}$:

$$V_{\sigma}(y) = \epsilon_{\sigma} V_s e^{-2y^2/w_s^2} \quad (\text{S19})$$

with $\epsilon_{\uparrow} = +1$ and $\epsilon_{\downarrow} = -1$;

3. the imaginary potential $iV_{\text{loss}}(y) = -i\hbar \frac{\Gamma(y)}{2}$ introduced in the effective Hamiltonian (S16), describing losses due to the scattering rate $\Gamma(y)$ defined by (S13) and proportional to $I(y)$.

Forward and backward scattering amplitudes associated with this complex potential are computed by solving the time-independent 1D Schrödinger equation with Numerov's method. Their square moduli are equal to the energy-dependent transmission $\mathcal{T}(E)$ and reflection $\mathcal{R}(E)$ respectively, and do not sum up to one since the total probability amplitude is not conserved by the non-unitary evolution. The loss probability $\mathcal{L}(E)$ is defined as the missing probability,

$$\mathcal{T}(E) + \mathcal{R}(E) + \mathcal{L}(E) = 1. \quad (\text{S20})$$

Landauer-Büttiker formula

In the Landauer-Büttiker picture presented in Fig. S2A, transport arises from the superposition of a right-moving and a left-moving current of particles with the Fermi-Dirac distributions $f_L(E)$ and $f_R(E)$ of the left and right reservoirs respectively, defined as:

$$f(E, \mu, T) = \frac{1}{1 + e^{\frac{E-\mu}{k_B T}}} \quad (\text{S21})$$

where $\mu = \mu_{L/R}$ and $T = T_{L/R}$ are the chemical potentials and temperatures of each reservoir. The net current is the difference between the currents transmitted through the mesoscopic channel with an energy-dependent probability $\mathcal{T}(E)$:

$$I_N = \frac{1}{h} \int_{-\infty}^{+\infty} [f_L(E) - f_R(E)] \mathcal{T}(E) dE. \quad (\text{S22})$$

It is dominated by the net transport of particles from the left reservoir at energies around the Fermi level where $f_L(E) \gg f_R(E)$.

Conductance is then obtained by dividing I_N by the chemical potential bias according to (S1).

We furthermore assume small biases $\Delta\mu$ relative to temperature $k_B T$ that simplifies the expression to

$$G = \frac{1}{h} \int_{-\infty}^{+\infty} \mathcal{T}(E) \left(-\frac{\partial f(E, \bar{\mu}, T)}{\partial E} \right) dE \quad (\text{S23})$$

with $\bar{\mu} = (\mu_L + \mu_R)/2$.

Extension to losses

This Landauer-Büttiker picture can be refined to estimate the losses incurred during the time evolution shown in Fig. 1.

In contrast to the net current (S22), the absolute particle number loss is equal to the sum of the currents lost from the mesoscopic channel by photon scattering with probability $\mathcal{L}(E)$,

$$-\frac{dN}{dt} = \frac{1}{h} \int_{-\infty}^{+\infty} [f_L(E) + f_R(E)] \mathcal{L}(E) dE \quad (\text{S24})$$

$$= \frac{1}{h} \int_{-\infty}^{+\infty} [f_L(E) - f_R(E)] \mathcal{L}(E) dE \quad (\text{S25})$$

$$+ \frac{2}{h} \int_{-\infty}^{+\infty} f_R(E) \mathcal{L}(E) dE. \quad (\text{S26})$$

It can be effectively split into a term (S25) similar to (S22) and a term (S26) representing particles below the Fermi level in both reservoirs which populate the mesoscopic channel and are therefore subject to losses, but do not contribute to a net current.

The time evolution of particle number N and internal energy U of each reservoir can be evaluated iteratively by (I) converting the extensive quantities ($N_{L,R}, U_{L,R}$) into

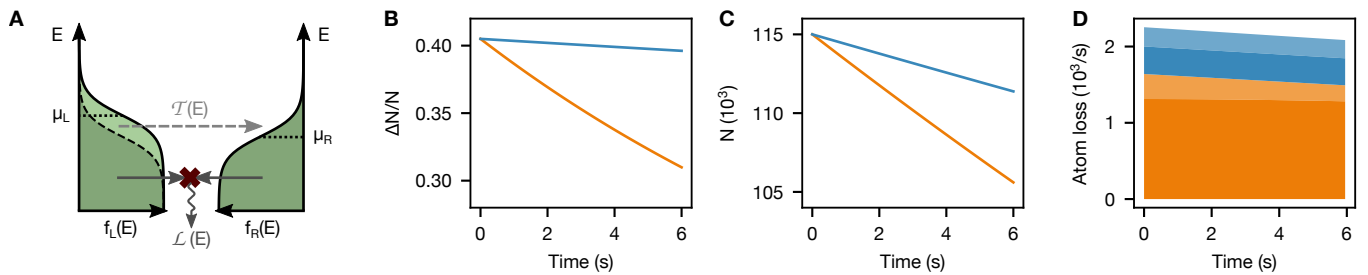


FIG. S2. **Landauer-Büttiker simulation of atom number evolution.** (A) In a Landauer-Büttiker picture and in the absence of a temperature bias, net transport can be attributed to the excess of particles in the left reservoir not compensated by the right reservoir [light green, Eq. (S22)] due to a chemical potential difference $\mu_L - \mu_R > 0$. On the other hand, losses involve the energy integration of the Fermi-Dirac distributions $f_L(E)$ and $f_R(E)$ of both reservoirs [Eq. (S24)], including states below the Fermi level that do not contribute to a net current [dark green, Eq. (S26)]. Conductance and loss are furthermore weighted by the energy-dependent transmission and loss coefficients of the mesoscopic channel $\mathcal{T}(E)$ and $\mathcal{L}(E)$ respectively. (B) Relative atom number difference $\Delta N/N$ and (C) Total atom number simulated for spin- \downarrow (orange) and spin- \uparrow (blue) with spin-dependent potential $V_s = k_B \cdot 0.25 \mu\text{K}$, gate potential $V_g = k_B \cdot 0.38 \mu\text{K}$, temperature $T = 60 \text{ nK}$ and initial conditions $N_0 = 115 \cdot 10^3$ and $\Delta N_0/N_0 = 0.41$. (D) Integrated losses for each spin associated to particles contributing [light color, Eq. (S25)] or not contributing [dark color, Eq. (S26)] to a net current. Losses occur mostly for \downarrow -atoms with the larger conductance and at energies below the Fermi level (dark orange).

chemical potential and temperature ($\mu_{L,R}, T_{L,R}$) using the equation of state of the non-interacting Fermi gas in a 3D harmonic trap [S5]; (II) inserting these quantities into the reservoir Fermi-Dirac distributions $f_{L,R}$ to compute the time-derivatives of particle number and energy in each reservoir:

$$\frac{dN_{L/R}}{dt} = \frac{1}{h} \int_{-\infty}^{+\infty} f_{R/L}(E) \mathcal{T}(E) dE - \frac{1}{h} \int_{-\infty}^{+\infty} f_{L/R}(E) [\mathcal{T}(E) + \mathcal{L}(E)] dE \quad (\text{S27})$$

$$\frac{dU_{L/R}}{dt} = \frac{1}{h} \int_{-\infty}^{+\infty} E \cdot f_{R/L}(E) \mathcal{T}(E) dE - \frac{1}{h} \int_{-\infty}^{+\infty} E \cdot f_{L/R}(E) [\mathcal{T}(E) + \mathcal{L}(E)] dE; \quad (\text{S28})$$

and (III) updating number and energy after a numerical time step using Euler's method.

We compute the time evolution of the thermodynamical quantities mentioned above for each spin separately and for realistic experimental parameters. The results are shown in Figs. S2B-D and are consistent with the experimental results in Figs. 1B,C. Losses are smaller for \uparrow -atoms which are blocked by the spin-dependent potential and therefore have lower densities in the dissipative region. Most of the losses (dark areas, Fig. S2D) actually concern atoms that are below the Fermi level (S26) and therefore do not affect conductance. The decrease of the reservoir chemical potential μ_{res} (not shown) is compatible with the experimental data (Fig. 1D) and is mitigated owing to the sublinear dependence of μ_{res} on the atom number $\mu_{\text{res}} \propto N^{1/3}$. We also predict temperature variations below 10 nK which indicate that Peltier effect and Joule heating are both negligible in the regime where the QPC is operated.

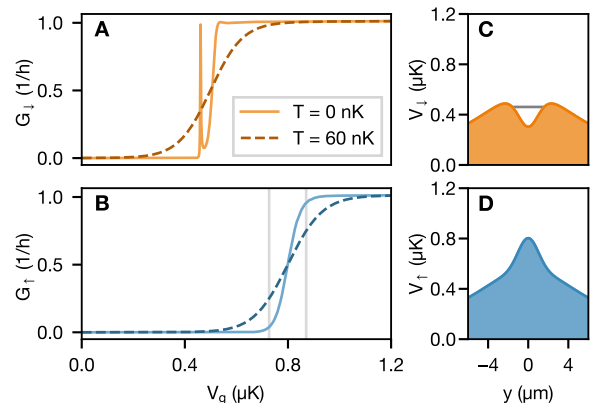


FIG. S3. **Temperature broadening of conductance features.** (A) Conductance for state \downarrow versus gate potential V_g , numerically evaluated for a spin-dependent potential $V_s = 0.25 \mu\text{K}$. A narrow resonance of full width at half maximum $2\Gamma_a \approx k_B \cdot 5 \text{ nK}$ is visible at zero temperature (solid line), indicating the existence of a bound state. It is blurred out at experimental temperatures of $T = 60 \text{ nK}$ (dashed line). (B) Conductance for state \uparrow , showing a step at $T = 0$ (solid line) which is broadened due to tunneling and above-barrier reflections within an energy range of about $k_B \cdot 0.14 \mu\text{K}$ (vertical gray lines). It is further broadened at $T = 60 \text{ nK}$ (dashed line). (C) Quasi-1D potential for state \downarrow and (D) for state \uparrow . The bound state created in the potential well experienced by \downarrow is indicated by a gray line.

CONDUCTANCE IN THE ABSENCE OF LOSSES

The spatial dependence of the spin-dependent potential $V_s(y)$ introduces new energy scales that could theoretically have an effect on transport.

For large enough negative potentials $-V_s$, the potential

well experienced by the attracted state $|\downarrow\rangle$ can accommodate a bound state weakly coupled to the reservoirs, thereby forming the cold-atom equivalent of a quantum dot. Its transmission for energies E close to the bound state energy E_a can be approximated by [S9]

$$\mathcal{T}(E) = \frac{1}{1 + \left(\frac{E-E_a}{\Gamma_a}\right)^2}, \quad (\text{S29})$$

where Γ_a is the tunneling energy from the bound state to either reservoir. We numerically compute the transmission of the actual potential landscape with $V_s = 0.25 \mu\text{K}$ and without dissipation, shown as a zero-temperature conductance in Fig. S3A (solid line). It features a resonance at energies below the classical potential barrier compatible with the existence of a bound state (Fig. S3C). It is however smoothed out at typical experimental temperatures $T = 60 \text{ nK}$ (dashed line in Fig. S3A) that are larger than the bound state coupling to the reservoirs, given by the resonance width $2\Gamma_a \approx k_B \cdot 5 \text{ nK} \approx h \cdot 100 \text{ Hz}$.

In contrast, positive potentials experienced by the repelled state $|\downarrow\rangle$ can be approximated by a parabolic barrier with transmission [S9]

$$\mathcal{T}(E) = \frac{1}{1 + e^{-2\pi \frac{E-E_b}{\hbar\Omega_b}}} \quad (\text{S30})$$

where E_b is the potential energy of the barrier and Ω_b its antitrapping frequency. This leads to a broadening of the zero-temperature conductance step by $2\hbar\Omega_b/\pi \approx k_B \cdot 0.14 \mu\text{K}$ (Fig. S3B, solid line) which is attributed to tunneling at energies below the barrier $E < E_b$ and above-barrier reflections for $E > E_b$. The broadening is also hidden at experimental temperatures (Fig. S3B, dashed line).

Note that losses are not included in Figs. S3A-B; we expect the transmission features to be further blurred out by dissipation for both attractive and repulsive potentials.

HARTREE MEAN-FIELD MODEL

Here, we detail how we model interaction effects on transport through the QPC at the mean-field level. In this description, a single particle is effectively embedded in the mean density of the other particles. Interactions introduce a shift of the single-particle energies which is proportional to the density and is used to calculate conductances within the Landauer framework.

Mean-field Hamiltonian

First we derive a mean-field Hamiltonian and self-consistent equations to calculate the densities inside the near-resonant tweezer. As we focus on the center of the

QPC, the transverse confinements and spin-dependent potential are uniform along the direction of transport. This leads to the following Hamiltonian consisting of kinetic and potential energy in second quantization

$$H_0 = \sum_{\sigma} \int \psi_{\sigma}^{\dagger}(\mathbf{r}) \left(-\frac{\hbar^2 \Delta}{2m} + V_{\sigma}(\mathbf{r}) \right) \psi_{\sigma}(\mathbf{r}) d^3\mathbf{r}, \quad (\text{S31})$$

where the field operator $\psi_{\sigma}(\mathbf{r})$ annihilates a particle with spin σ at position \mathbf{r} . The potential is given by

$$V_{\sigma}(\mathbf{r}) = \frac{1}{2}m\omega_x^2 x^2 + \frac{1}{2}m\omega_z^2 z^2 + V_{\sigma} \quad (\text{S32})$$

where $\omega_{x,z} = 2\pi \cdot \nu_{x,z}$. The interparticle interactions for ultracold atoms are of the contact type and captured by the Hamiltonian

$$H_{\text{int}} = \frac{g}{2} \sum_{\sigma} \int \psi_{\sigma}^{\dagger}(\mathbf{r}) \psi_{\bar{\sigma}}^{\dagger}(\mathbf{r}) \psi_{\bar{\sigma}}(\mathbf{r}) \psi_{\sigma}(\mathbf{r}) d^3\mathbf{r} \quad (\text{S33})$$

with the interaction constant $g = 4\pi\hbar^2 a/m$ at scattering length a . As both spin species are summed the prefactor is necessary to avoid double counting. Due to Pauli's principle a particle with spin σ only interacts with one of opposite spin $\bar{\sigma}$.

Basis change

As the channel provides harmonic confinement in transverse directions and free motion in longitudinal direction, it is convenient to change the basis states via

$$\psi_{\sigma}(\mathbf{r}) = \sum_{\mathbf{n}k} \phi_{n_x}(x) \phi_{n_z}(z) \frac{1}{\sqrt{L}} e^{iky} a_{\mathbf{n}k\sigma}. \quad (\text{S34})$$

Here, we label the harmonic transverse modes with a multi-index $\mathbf{n} = (n_x, n_z)$ and the longitudinal plane wave with the wavenumber k that is a multiple of $2\pi/L$. The harmonic eigenstates along the x axis are

$$\phi_{n_x}(x) = \frac{1}{(\pi a_x^2)^{1/4}} \frac{1}{\sqrt{2^{n_x} n_x!}} \cdot e^{-x^2/2a_x^2} \cdot H_{n_x}(x/a_x) \quad (\text{S35})$$

with the Hermite polynomials H_n of order n and the natural length $a_x = \sqrt{\hbar/m\omega_x}$. The formula reads analogously along the z axis.

Now, we rewrite the Hamiltonians H_0 and H_{int} in this basis and only keep the lowest transverse mode $\mathbf{n} = \mathbf{0}$ as we work in the single-mode regime. Then, the Hamiltonian H_0 operating on the single-particle space becomes

$$H_0^{\text{sm}} = \sum_{k\sigma} \left[\frac{\hbar^2 k^2}{2m} + V_0 + V_{\sigma} \right] a_{\mathbf{0}k\sigma}^{\dagger} a_{\mathbf{0}k\sigma} \quad (\text{S36})$$

with the energy $V_0 = \hbar\omega_x/2 + \hbar\omega_z/2$ in the transverse direction. The interaction Hamiltonian H_{int} is cast into

$$H_{\text{int}}^{\text{sm}} = \frac{g}{2} \sum_{\sigma} \sum_{\substack{k_1 k_2 \\ k_3 k_4}} \frac{\text{ov}}{a_x a_z L} \frac{1}{L} \delta_{k_1+k_2, k_3+k_4} \times \\ \times a_{\mathbf{0}k_1\sigma}^{\dagger} a_{\mathbf{0}k_2\bar{\sigma}}^{\dagger} a_{\mathbf{0}k_3\bar{\sigma}} a_{\mathbf{0}k_4\sigma}. \quad (\text{S37})$$

The spatial integration along y reduces to the Kronecker delta $\delta_{k_1+k_2, k_3+k_4}$ which ensures momentum conservation. The integration over the x and z directions gives rise to the overlap

$$\text{ov} = \int_{-\infty}^{\infty} \varphi_0^A(\xi) d\xi \cdot \int_{-\infty}^{\infty} \varphi_0^A(\xi) d\xi = \frac{1}{2\pi} \quad (\text{S38})$$

with the dimensionless wavefunction $\varphi_0(\xi) = \sqrt{a_x} \cdot \phi_0(\xi a_x)$ and reduced coordinates $\xi = x/a_x$, and analogously along the z axis.

As we focus on a single transverse mode and elastic collisions are restricted to 1D the individual particle momenta are preserved along y ($k_1 = k_4$, $k_2 = k_3$). Hence, the interaction Hamiltonian simplifies to

$$H_{\text{int}}^{\text{sm}} = \frac{g}{2} \sum_{\sigma} \sum_{k_1 k_2} \frac{\text{ov}}{a_x a_z} \frac{1}{L} a_{\mathbf{0}k_1\sigma}^{\dagger} a_{\mathbf{0}k_2\bar{\sigma}}^{\dagger} a_{\mathbf{0}k_2\bar{\sigma}} a_{\mathbf{0}k_1\sigma}. \quad (\text{S39})$$

As the operators a_{α} and a_{α}^{\dagger} obey anti-commutation relations the product of operators in the Hamiltonian can be brought into the form $a_{\alpha}^{\dagger} a_{\alpha} a_{\beta}^{\dagger} a_{\beta}$. By applying the mean-field approximation in the density operators $a_{\alpha}^{\dagger} a_{\alpha}$ and $a_{\beta}^{\dagger} a_{\beta}$ we obtain

$$H_{\text{int}}^{\text{MF}} = \sum_{\sigma} \sum_k \left(\frac{\hbar^2 k^2}{2m} + \varepsilon_{\sigma} \right) a_{\mathbf{0}k\sigma}^{\dagger} a_{\mathbf{0}k\sigma} + E_0 \quad (\text{S40})$$

with the energy ε_{σ} that includes the transverse energy, the spin-dependent potential, and the interaction shift

$$\varepsilon_{\sigma} = V_0 + V_{\sigma} + \frac{1}{L} \sum_{k'} U \langle a_{\mathbf{0}k'\bar{\sigma}}^{\dagger} a_{\mathbf{0}k'\bar{\sigma}} \rangle \quad (\text{S41})$$

and an energy offset E_0 that avoids overcounting:

$$E_0 = -\frac{1}{2L} \sum_{\sigma} \sum_{kk'} U \langle a_{\mathbf{0}k\sigma}^{\dagger} a_{\mathbf{0}k\sigma} \rangle \langle a_{\mathbf{0}k'\bar{\sigma}}^{\dagger} a_{\mathbf{0}k'\bar{\sigma}} \rangle. \quad (\text{S42})$$

Here, the coupling constant is $U = g \cdot \text{ov}/(a_x a_z)$. The mean-field Hamiltonian is diagonal in the occupation operator $a_{\alpha}^{\dagger} a_{\alpha}$ which simplifies the following treatment.

Density calculation

Based on the mean-field Hamiltonian (S40) we derive formulae for the mean density and its variance and pinpoint when particles start to enter the tweezer. With these expressions we discuss the situation at our experimental parameters.

Mean density

The line density of each spin state is obtained from the occupation numbers by summing over the wavenumber.

$$n_{\sigma} = \frac{1}{L} \sum_k \langle a_{\mathbf{0}k\sigma}^{\dagger} a_{\mathbf{0}k\sigma} \rangle \quad (\text{S43})$$

For a diagonal Hamiltonian the occupation number is given in the grand canonical ensemble by

$$\langle a_{\mathbf{0}k\sigma}^{\dagger} a_{\mathbf{0}k\sigma} \rangle = f \left(\beta \left[\frac{\hbar^2 k^2}{2m} + \varepsilon_{\sigma} - \mu_{\sigma} \right] \right) \quad (\text{S44})$$

with the Fermi-Dirac distribution $f(x) = 1/(1 + e^x)$, the inverse temperature $\beta = 1/k_B T$ and the chemical potential μ_{σ} of spin state σ imposed by the reservoirs. In the thermodynamic limit ($L \rightarrow \infty$), the summation becomes an integral over the wavenumber which can be transformed into an integral over energy to arrive at the expression

$$n_{\sigma} = \frac{1}{\lambda} F_{-1/2}(\beta [\mu_{\sigma} - \varepsilon_{\sigma}]), \quad (\text{S45})$$

where F_j denotes the complete Fermi-Dirac integral of order j [S10, Eq. (25.12.14)] and λ the thermal wavelength given by

$$\lambda = \sqrt{\frac{2\pi\hbar^2}{mk_B T}}. \quad (\text{S46})$$

The energy ε_{σ} defined in (S41) can be written with equation (S43) as

$$\varepsilon_{\sigma} = V_0 + V_{\sigma} + U n_{\bar{\sigma}}. \quad (\text{S47})$$

The single-particle energy ε_{σ} depends on the density of the opposite spin and, together with the equation of state (S45), forms a system of equations for the line density that needs to be solved self-consistently.

Density variance

To estimate the fluctuations around the mean line density we start with the particle number fluctuations in the grand canonical ensemble [S11] that is valid for all system sizes:

$$\langle N_{\sigma}^2 \rangle - \langle N_{\sigma} \rangle^2 = k_B T \left(\frac{d\langle N_{\sigma} \rangle}{d\mu_{\sigma}} \right)_T. \quad (\text{S48})$$

The particle number fluctuations are converted into fluctuations of the densities via $\hat{N}_{\sigma} = L \hat{n}_{\sigma}$ giving

$$\langle n_{\sigma}^2 \rangle - \langle n_{\sigma} \rangle^2 = \frac{k_B T}{L} \left(\frac{d\langle n_{\sigma} \rangle}{d\mu_{\sigma}} \right)_T. \quad (\text{S49})$$

It is visible that fluctuations are stronger with increasing temperature and for smaller systems. The variation of densities with chemical potential contains the fermionic particle statistics and the interparticle interactions.

Density onset at zero temperature

At zero temperature, equation (S45) simplifies to

$$n_{\sigma} = \sqrt{\frac{2m}{\pi^2 \hbar^2}} \cdot \theta(\mu - \varepsilon_{\sigma}) \cdot \sqrt{\mu - \varepsilon_{\sigma}} \quad (\text{S50})$$

with the Heaviside step function θ and chemical potential μ equal for both spin states ($\mu_\uparrow = \mu_\downarrow$). The density displays the square root behavior in chemical potential expected from the $1/\sqrt{E}$ proportionality of the one-dimensional system's density of states. At small chemical potentials, only the state $|\downarrow\rangle$ attracted by the tweezer occupies the channel and hence its density is unaffected by interactions. It reads

$$n_\downarrow = \sqrt{\frac{2m}{\pi^2 \hbar^2}} \cdot \theta(\mu - V_0 - V_\downarrow) \cdot \sqrt{\mu - V_0 - V_\downarrow}. \quad (\text{S51})$$

Clearly, the particles in state $|\downarrow\rangle$ start to occupy the channel at the chemical potential $\hat{\mu}_\downarrow = V_0 + V_\downarrow$. The threshold of the other state depends on interactions and follows from formula (S50) via $\hat{\mu}_\uparrow - \varepsilon_\uparrow = 0$ that is

$$\hat{\mu}_\uparrow - V_0 - V_\uparrow - U n_\downarrow = 0. \quad (\text{S52})$$

Together with equation (S51) this forms a self-consistent equation for $\hat{\mu}_\uparrow$. The solution is

$$\hat{\mu}_\uparrow = V_0 + V_\uparrow + \Delta\mu_{\text{int}}, \quad (\text{S53})$$

$$\Delta\mu_{\text{int}} = 2u^2 + 2u\sqrt{u^2 + V_\uparrow - V_\downarrow} \quad (\text{S54})$$

with the scaled coupling constant

$$u = \sqrt{\frac{m}{2\pi^2 \hbar^2}} U. \quad (\text{S55})$$

Results and discussion

Fig. S4 displays the density n_σ versus chemical potential μ for both spin states at two temperatures and scattering lengths obtained using equation (S45). The non-interacting predictions are presented as dashed curves and, as expected, they follow a square root behavior at low temperatures. At the chemical potential $\hat{\mu}_\downarrow$, particles attracted by the tweezer start to enter the channel. Its location is independent of interactions as particles of the other state are absent. This is valid if the effective Zeeman splitting avoids thermal occupation, meaning when $V_\uparrow - V_\downarrow \gg k_B T$. The onset $\hat{\mu}_\uparrow$ where the other state occupies the tweezer is shifted towards smaller (larger) chemical potentials with attractive (repulsive) interactions. The shift is quantified by $\Delta\mu_{\text{int}}$ in equation (S54) that is asymmetric in interactions. It is larger in the repulsive regime ($a > 0$) than in the attractive case with opposite scattering length $-a$. That is because the energies ε_σ change linearly with the densities while the densities behave nonlinearly with chemical potential. The asymmetry is typically small for our experimental parameters. For example in Fig. S4 the shifts $\Delta\mu_{\text{int}}$ are $k_B \cdot 54$ nK for a scattering length of $800 a_0$ and $-k_B \cdot 48$ nK for $-800 a_0$ respectively. Besides the onset locations, the densities themselves also deviate from the non-interacting expectation with interactions when both spin states are present

in the tweezer. Attractive interactions increase the densities while they are reduced with repulsion.

The density fluctuations are indicated with the standard deviation (shaded regions) and are larger at higher temperatures. They are useful to check if they are indeed small as assumed by the mean-field theory. At our typical temperature of 66 nK the fluctuations only dominate at small chemical potentials and are moderate compared to the mean density when particles enter the tweezer. Hence despite the small system size we expect mean-field theory to be valid within the interesting chemical potential range.

Conductance calculation

In the following we determine conductances including interactions via the modified densities. We start with the Landauer formula assuming infinitesimal bias between the reservoirs and classical transmission through the QPC:

$$G_\sigma = \frac{1}{h} f(\beta[\mu_\sigma - \hat{\varepsilon}_\sigma]). \quad (\text{S56})$$

The conductances are related to the single-particle energies $\hat{\varepsilon}_\sigma$ that are modified by interactions as ε_σ but additionally consider the non-locality of transport. While the energies ε_σ are related to the center, transport is dominated by the maxima in the effective potential that may be off-centered, as shown in Fig. S5. Assuming everywhere the same density as at the center, the doubly-modified single-particle energies are

$$\hat{\varepsilon}_\sigma = \hat{V}_0 + \hat{V}_\sigma + U n_{\hat{\sigma}} \quad (\text{S57})$$

where the transverse energy \hat{V}_0 and spin-dependent potential \hat{V}_σ are obtained by evaluating (S18) and (S19) at the maxima locations y_σ .

Results and discussion

Fig. S6 shows the conductance G_σ versus chemical potential μ for the same conditions as for the densities in graph S4. Upon increasing the chemical potential the attracted state $|\downarrow\rangle$ starts to occupy the tweezer beyond the density onset $\hat{\mu}_\downarrow$ (vertical blue line). However, due to the shape of the effective potential, shown in Fig. S5, conductance rises later and the transition is centered around the vertical gray line. As expected, the transition of state $|\uparrow\rangle$ agrees with the density onset $\hat{\mu}_\uparrow$ and is modified by interactions. For comparison the non-interacting predictions are shown at the same temperatures (dashed curves). From the conductance curves the chemical potential separation between the two states is extracted at half conductance quantum $1/2h$, as plotted in Fig. 4.

Additionally to interactions, dissipation influences the separation as well. In principle it can be included in

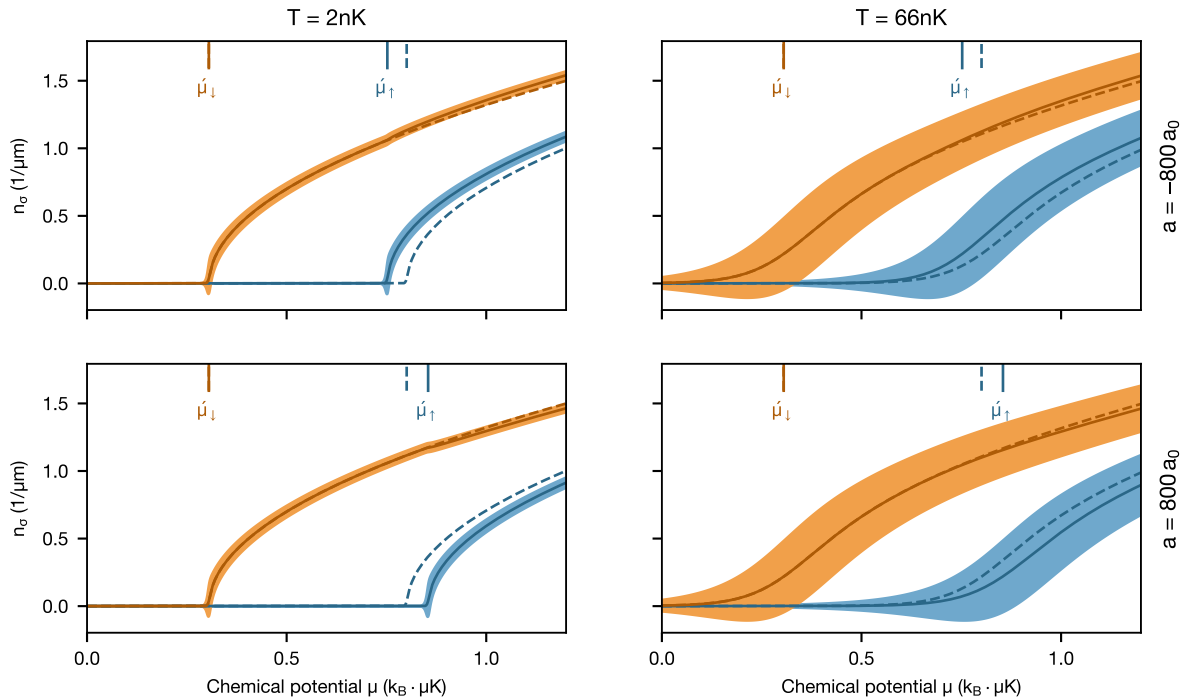


FIG. S4. **Self-consistent line density.** Density n_σ as a function of chemical potential μ equal for both spin states at different temperatures T and scattering lengths a ($|\downarrow$) in orange and $|\uparrow$) in blue). The shaded regions indicate the standard deviation (S49) estimated in the grand canonical ensemble for a system size $L = w_s = 2.0 \mu\text{m}$. For comparison the non-interacting predictions are shown at the same temperature (dashed curves). The vertical lines indicate the chemical potential onsets $\hat{\mu}_\sigma$ at zero temperature with (solid line) and without interactions (dashed line). The spin-dependent potential V_σ is $k_B \cdot \pm 248 \text{ nK}$ and the transverse trapping frequencies are $\omega_x = 2\pi \cdot 14.0 \text{ kHz}$ and $\omega_z = 2\pi \cdot 9.03 \text{ kHz}$.

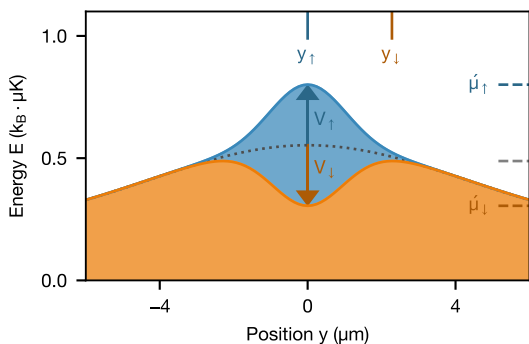


FIG. S5. **Effective one-dimensional potential.** The horizontal colorful lines indicate the density onsets $\hat{\mu}_\sigma$ at zero temperature and without interactions and in gray the shifted conductance transition due to the effective potential. The experimental parameters are as for Fig. S4.

the mean-field description using for example the quantum jump approach [S12]. Here, we discuss dissipation qualitatively considering only its effect on the densities. The particle losses will overall reduce conductances but the location of the first transition will remain fixed as the chemical potential is imposed by the reservoirs and interactions have no effect. At the second transition the density n_\downarrow is reduced by dissipation, which should also reduce the absolute shift compared to the non-interacting case.

[S1] C. H. Schunck, M. W. Zwierlein, C. A. Stan, S. M. F. Raupach, W. Ketterle, A. Simoni, E. Tiesinga, C. J.

Williams, and P. S. Julienne, *Feshbach resonances in fermionic ^6Li* , *Physical Review A* **71**, 045601 (2005).

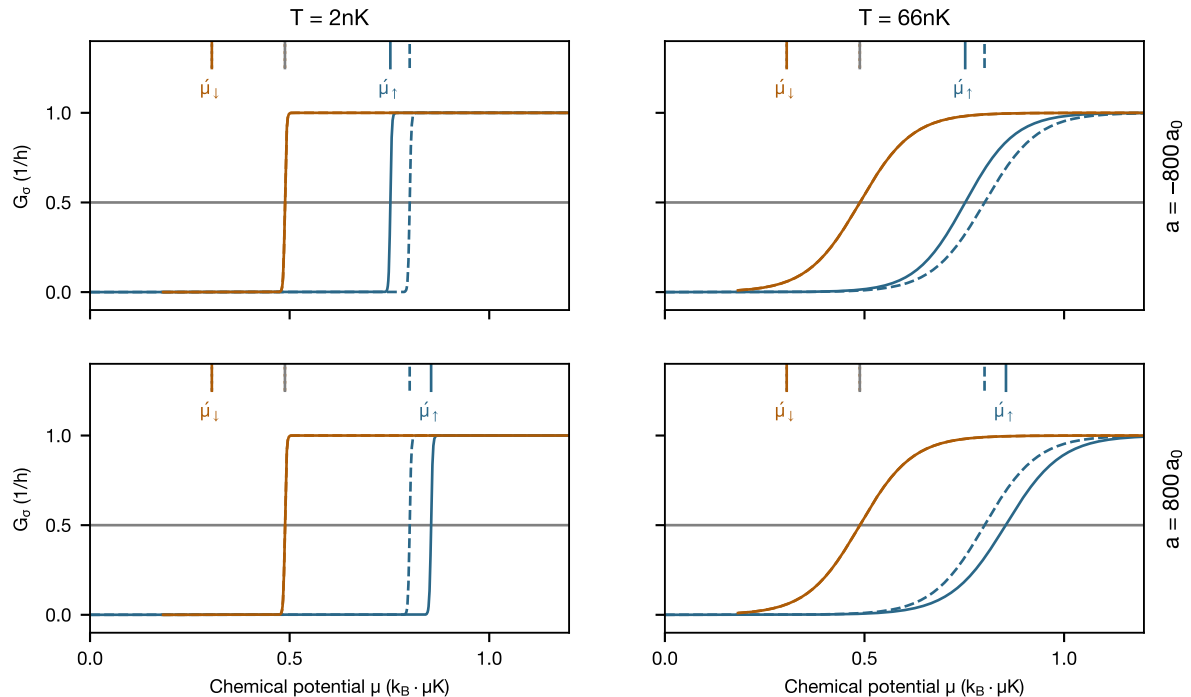


FIG. S6. **Conductance with mean-field interactions.** Conductance G_σ versus chemical potential μ equal for both spin states at different temperatures T and scattering lengths a (\downarrow in orange and \uparrow in blue). Non-interacting predictions are shown at the same temperature (dashed curves). The vertical colorful lines indicate the density onsets $\dot{\mu}_\sigma$ at zero temperature with (solid line) and without interactions (dashed line) and in gray the shifted onset due to the effective potential. The experimental parameters are as for Fig. S4.

- [S2] S. Häusler, S. Nakajima, M. Lebrat, D. Husmann, S. Krinner, T. Esslinger, and J.-P. Brantut, *Scanning Gate Microscope for Cold Atomic Gases*, *Physical Review Letters* **119**, 030403 (2017).
- [S3] P. T. Boggs and J. E. Rogers, *Orthogonal distance regression*, *Contemporary Mathematics* **112**, 183 (1990).
- [S4] S. Krinner, M. Lebrat, D. Husmann, C. Grenier, J.-P. Brantut, and T. Esslinger, *Mapping out spin and particle conductances in a quantum point contact*, *Proceedings of the National Academy of Sciences* **113**, 8144 (2016).
- [S5] G. Su, J. Chen, and L. Chen, *Low-temperature behavior of a weakly interacting Fermi gas trapped in a power-law potential*, *Physics Letters A* **315**, 109 (2003).
- [S6] M. E. Gehm, Ph.D. thesis, Duke University (2003).
- [S7] S. Krinner, D. Stadler, D. Husmann, J.-P. Brantut, and T. Esslinger, *Observation of quantized conductance in neutral matter*, *Nature* **517**, 64 (2015).
- [S8] C.-C. Chien, M. Di Ventra, and M. Zwolak, *Landauer, Kubo, and microcanonical approaches to quantum transport and noise: A comparison and implications for cold-atom dynamics*, *Physical Review A* **90**, 023624 (2014).
- [S9] T. Ihn, *Semiconductor Nanostructures: Quantum states and electronic transport* (Oxford University Press, Oxford, New York, 2009).
- [S10] F. W. J. Olver, D. W. Lozier, R. F. Boisvert, and C. W. Clark, *NIST handbook of mathematical functions* (Cambridge University Press, 2010).
- [S11] J. Stephenson, *Fluctuations in particle number in a grand canonical ensemble of small systems*, *American Journal of Physics* **42**, 478 (1974).
- [S12] K. Mølmer, Y. Castin, and J. Dalibard, *Monte carlo wave-function method in quantum optics*, *J. Opt. Soc. Am. B* **10**, 524 (1993).